



# Influence of non-erodible particles with multimodal size distribution on aeolian erosion of storage piles of granular materials

C. L. de Morais<sup>1</sup> · M. C. S. Ferreira<sup>1,2</sup> · J. M. Santos<sup>1</sup> · B. Furieri<sup>1</sup> · J.-L. Harion<sup>3</sup>

Received: 4 May 2018 / Accepted: 15 October 2018 / Published online: 22 October 2018  
© Springer Nature B.V. 2018

## Abstract

Aeolian erosion of granular materials is investigated by means of a mathematical emission model and experimental wind tunnel measurements. Main model input data are: friction velocity, relationship between cover rate (CR) and eroded height (H) and particle properties (density, size distribution). It is proposed: (1) to evaluate the linearity of the relation between CR and H considering the presence of a multimodal distribution of particle sizes, (2) to validate the mathematical model with wind tunnel data, (3) to evaluate the protective effect of non-erodible particles and (4) to qualitatively evaluate the final stage of erosion through experimental photographs of the oblong stockpile. The relationship between CR and H may still be considered linear for the tested mixture of particles. The modelled emission, when compared with experimental data, showed that the physical tendency of the aeolian erosion phenomenon was well predicted. The model showed to be useful in comparative analysis between scenarios but not in absolute values due to errors found. It is valid for the monitoring of air quality degradation due to aeolian erosion of open yards of storage piles. Detailed analysis of emitted mass explained that the smallest diameters among the non-erodible particles create a less effective protection effect leading to higher emissions. The qualitative analysis of high-quality photographs of the experiments showed that the non-erodible particle agglomeration on the stockpile surface can be well explained if one evaluates simultaneously, on the pile, the angle of velocity vectors (which influences the threshold friction velocity value) and shear stress.

**Keywords** Aeolian erosion · Emission model · Non-erodible particles · Wind tunnel

---

✉ B. Furieri  
bruno.furieri@ufes.br

<sup>1</sup> Department of Environmental Engineering, Universidade Federal do Espírito Santo, 514, Av. Fernando Ferrari, Vitória, ES, Brazil

<sup>2</sup> Department of Mathematics, Instituto Federal do Espírito Santo, 1729, Av. Vitória, Vitória, ES, Brazil

<sup>3</sup> Research Centre, Institut Mines-Télécom Lille Douai, 764, boulevard Lahure, 59500 Douai, France

## 1 Introduction

Many factors influence the emission of granular materials from stockpiles exposed to wind erosion: material density, moisture, particles size distribution, stockpile shape, wind velocity, saltation and the availability of erodible particles [1]. The most widely used model for estimating emissions due to wind erosion of stockpiles has been proposed by the United States Environmental Protection Agency [37]. However, a major limitation of this model is that it neglects the proportion of erodible and non-erodible particles in the mixture of granular materials. Efforts have been made to develop new emission models that include the effect of non-erodible particles, but they were mainly built for estimating emissions on relatively flat erodible surfaces [7, 18, 21, 22, 38].

The model developed by Descamps et al. [7] described the temporal evolution of particle emissions for a bed containing erodible and non-erodible particles exposed to a turbulent flow, but assumed that the emission would cease when the surface is only covered by non-erodible particles, e.g., neglecting the pavement effect in which non-erodible particles serve to protect erodible particles causing emission to cease before all erodible particles are emitted. Kok et al. [22] have developed an analytical expression for particles entrained by a bed containing erodible soils in which the number of erodible particles is unlimited, but this is only the case for a single size particle. On the other hand, their model takes into account the saltation phenomenon that can influence the emission of other particles caused by the impact of particles being transferred back to the surface. In addition, the cohesion between the particles of smaller diameters was also considered which is important for very small particles. Klose et al. [21] proposed a model incorporating cohesion due to the effects of moisture and the influence of non-erodible elements on emission. However, the model was not compared with experimental results. Zou et al. [38] proposed a conceptual model of particles emitted from a bed of granular material of multimodal particle size distributions and additional contents e.g., (e.g., salt and organic matter, net water, frozen water, snow cover, plant roots, vegetation and gravel cover), which were expressed as a function of shear force. However, as in the work of Klose et al. [21], the estimation was theoretical, having no experimental basis.

Hoonhout and De Vries [18] modelled emissions for a spatial and temporal variation of particle size distributions and erodibility over a bed of particles due to wind erosion. Their model employs an advection scheme using a transport equation through the discretization of the bed in horizontal and vertical cells to account for spatial variations in bed surface properties. They compared their results with hypothetical case studies and wind tunnel experimental data [9, 31] from the literature. The main conclusion was that deeper numerical and experimental investigation was needed before this model could be used for estimating erosion from storage piles.

Other researchers have investigated the pavement effect created by the increase in non-erodible elements by conducting laboratory experiments. Most of them have considered the shear stress partitioning over a bed of particles by dividing the shear stress between non-erodible elements and the surrounding surface [5, 12, 15, 17, 19, 25, 26, 28, 33, 35]. The results of these studies confirm that larger diameter particles create zones of low shear downstream where it is not possible to achieve the minimum friction velocity required for the particles emission. Computational Fluid Dynamics has emerged as an alternative to the experimental approaches. Turpin et al. [36] carried out numerical simulations to model the pavement process using shear stress partitioning concepts for beds containing non-erodible elements (represented by roughness elements) and to investigate the magnitude of friction

velocity on the erodible surface in the presence of the non-erodible elements. Their results show good agreement with previous experimental studies [5, 15, 16, 24, 25, 27, 30]. Furi-eri et al. [13] also performed similar numerical simulations to estimate the shear stress distribution over a bed of erodible and non-erodible particles, but these authors considered a polydispersed distribution of rough element sizes for the same initial cover rates (proportion of non-erodible particles covering the surface) used by Turpin et al. [36] (up to 12%). The results showed that the equation proposed by Turpin et al. [36] remains valid even for a polydispersed distribution.

In order to fill the gap left by the emission model of Descamps et al. [7] and making use of the shear stress partition model proposed by Turpin et al. [36] and Caliman [3] proposed a model that includes the pavement phenomenon occurring for final cover rates < 100%. Furthermore, Caliman [3] adapted the model to estimate emissions from stockpiles and found a fair agreement between the calculated emitted mass and the emitted mass measured experimentally in a wind tunnel experiment. It was assumed that cover rate is linearly related to the eroded height (i.e., the depth of soil loss). However, it was not tested for a multimodal distribution of erodible and non-erodible particles with three modes (previous papers evaluated this condition for two modes). The present paper aims to test the emission model for a multimodal particle size distribution in which: (1) one mode is always erodible (for the tested velocities), (2) a second mode is always non-erodible and (3) a third mode has its erodibility varying with the incident wind velocity.

It is important to consider that if a second larger particle diameter of non-erodible particles is present in a mixture, the emission rate is expected to decrease, because they generate a more effective protection effect. However, if this second non-erodible particle diameter is smaller, the opposite is expected, the particles would generate a lower protection effect, leading to higher emissions. So, a multimodal distribution of particles diameters, which is found in real stockpiles can alter the pavement effect on emission rate.

The present paper aims to evaluate the influence of a multimodal size distribution of non-erodible particles on beds and stockpiles emission using the model proposed by Caliman [3], and to verify the model performance for different wind velocities. Emission model results are compared with experimental data of lost mass from model piles from wind tunnel experiments. Besides that, a qualitative analysis of the final surface particle size distributions of a stockpile is made using high-quality images recorded during wind tunnel testing.

## 2 Emission model

Caliman [3] proposed an emission model for beds using a simple equation that calculates the emitted mass from knowledge of the emitted volume:

$$E_f = (1 - \alpha_{NE}) \rho_{bed} H_f S_{bed} \quad (1)$$

where  $\alpha_{NE}$  is the mass fraction of non-erodible particles [ $kg_{NE}/kg_{mixture}$ ],  $\rho_{bed} = \varphi \rho_P$  [ $kg_{mixture}/m^3_{bed}$ ],  $\varphi$  is the volumetric fraction of the mixture in the bed [ $m^3_{mixture}/m^3_{bed}$ ] (mixture represents the diameters that compose the bed. The mixture could be arranged in another structure, for example, in a stockpile),  $\rho_P$  is the particle density [ $kg_{mixture}/m^3_{mixture}$ ],  $H_f$  is the final eroded height of the bed [m] and  $S_{bed}$  is bed area [ $m^2$ ].

In order to estimate  $H_f$ , it was necessary to find an equation that relates the cover rate and eroded height. Figure 1 shows the evolution of the surface ratio occupied by non-erodible

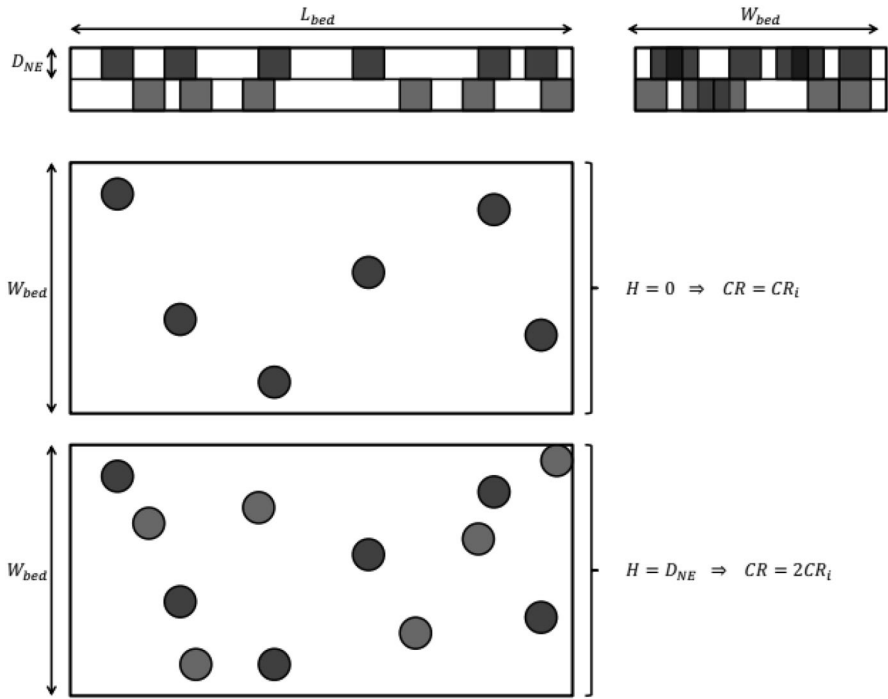


**Fig. 1** Evolution of the surface covering by non-erodible particles ( $CR$ ) as a function of the eroded height ( $H$ ). The width ( $W_{bed}$ ) and length ( $L_{bed}$ ) of the bed are shown

particles ( $CR$ ) as a function of eroded height ( $H$ ) for a uniform distribution of non-erodible particle sizes proposed by Caliman [3]. The Shao and Lu [34] emission criterion was used to determine the erodibility of the particles:

$$u_{*f} = 0,11 \sqrt{\frac{\rho_p - \rho}{\rho} gD + \frac{\gamma}{\rho D}} \tag{2}$$

where  $u_{*f}$  is the particle threshold friction velocity [m/s],  $\rho$  is the air density [kg/m<sup>3</sup>],  $D$  is the particles diameter [m],  $g$  is the acceleration due to gravity [m/s<sup>2</sup>] and  $\gamma$  is surface energy that characterizes cohesion [N/m].

From Fig. 1, considering that the mean height of an element ( $D_{NE}$ ) is equal to the eroded height of each layer removed during erosion and that the particles are distributed in the same proportion in each layer, the ratio between  $CR$  and  $H$  is:

$$CR = aH + CR_i \tag{3}$$

where  $CR_i$  is the initial cover rate. Therefore,  $H_f$  can be calculated as a function of  $CR_f$ .

The line slope is then calculated as:

$$a = \frac{CR_f - CR_i}{H_f} \tag{4}$$

where the initial cover rate, according to Caliman [3]’s experimental data and assuming that the non-erodible particles are homogeneously distributed in the mixture, is equivalent to:

$$CR_i = \alpha_{NE} \varphi \tag{5}$$

In order to consider the effects of pavement, we used the equation proposed by Turpin et al. [36] (Eq. 6) to assess the evolution of the friction velocity of the erodible surface as a function of the cover rate and shape of the non-erodible particles.

$$1 - R_{fric} = A(CR)^M (S_{frontal}/S_{floor})^N \tag{6}$$

where  $R_{fric}$  is defined by Eq. (7),  $S_{frontal}$  is the frontal area of the elements [m<sup>2</sup>],  $S_{floor}$  is the basal area of the elements [m<sup>2</sup>] and  $A$ ,  $M$  and  $N$  are constants found by means of numerical simulations to calculate the friction velocities  $u_{*r}$  on a surface containing the roughness elements (non-erodible particles). In the present work we used the constants  $A$ ,  $M$  and  $N$  calculated by Caliman [3].

$$R_{fric} = \frac{u_{*r}}{u_{*s}} \tag{7}$$

where  $u_{*r}$  is the mean friction velocity on an erodible surface under the roughness influence [m/s] and  $u_{*s}$  is the mean friction velocity [m/s] on a smooth surface.

The rate  $S_{frontal}/S_{floor}$  for cylindrical elements is given by:

$$\frac{S_{frontal}}{S_{floor}} = \frac{4}{\pi} \frac{H}{D_{NE}} \tag{8}$$

Therefore, considering Eqs. (3) and (6) becomes:

$$1 - R_{fric} = A(aH + CR_i)^M \left( \frac{4H}{\pi D_{NE}} \right)^N \tag{9}$$

and considering that in the erosion final stage  $R_{fric}$  is minimal, the equation becomes:

$$1 - R_{MIN} = A(aH_f + CR_i)^M \left( \frac{4H_f}{\pi D_{NE}} \right)^N \tag{10}$$

So  $H_f$  can be calculated and the emitted mass estimated by Eq. (1).

Caliman [3] also proposed an adaptation of the emission model for stockpiles. The inclined surface of the stockpile (ascending or descending) causes a strong influence of the gravity force on the emission. Caliman [3] calculated the angles  $\theta$  at which the fluid flows over the surface and, depending on this angle, the particles friction velocity threshold (emission criterion) is modified in relation to the value it would have for a flat bed.

The angle  $\theta$  is defined by:

$$\theta = \arcsin (\tau_z/\tau) \tag{11}$$

where  $\tau_z$  [Pa], is the vertical component of the shear stress.

The shear stresses distribution on an oblong stockpile was calculated similarly to the works of many authors [1, 2, 4, 6, 8, 10, 11, 14, 32, 36].

To re-evaluate the particle emission criterion according to  $\theta$ , the Iversen and Rasmussen [20] equation is used:

$$\frac{u_{*t}(\theta)^2}{u_{*t}(0)^2} = \cos \theta + \frac{\sin \theta}{\tan \xi} \quad (12)$$

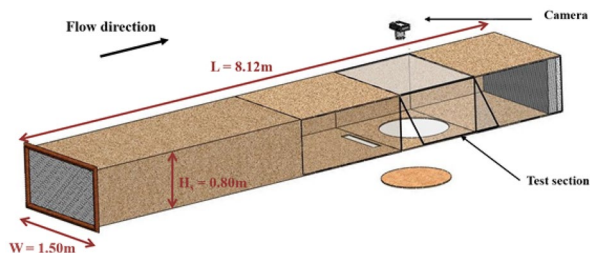
where  $\xi$  is the internal friction angle. The idea of the model proposed by Caliman [3] is to separate the stockpile into isosurfaces that have the same emission criteria. So, each isosurface could be considered as a bed and then the model could be applied.

### 3 Experimental study

Wind tunnel experiments were carried out in the Department of Industrial Energy (IMT Lille Douai, France). Several roughness elements were placed upstream of the test section of the wind tunnel allowing the formation of a turbulent boundary layer. The thickness of the boundary layer ( $\delta$ ) in the test section was sufficiently larger than the height of the stockpile ( $\delta = 16$  cm and  $h = 7.7$  cm, respectively). The flow rate was controlled by an axial fan located downstream of the wind tunnel. A high-quality photo camera (Nikon D-100) was installed at the top of the test section (transparent glass wall) to record the evolution of the erosion process. The resolution of the photographs is  $3648 \times 2650$  pixels. The area visualized by the camera was concentrated on the stockpile. This system is capable of visualizing extremely detailed distribution of particles over the sand stockpile model surface. A weighing system was placed inside an airtight box underneath the test section that recorded the mass of the stockpile in the wind tunnel. The weighing device was the electronic balance BEL Engineering Mark K30.1, which has a resolution of 0.1 g. The wind tunnel set-up is shown in Fig. 2. Further details of the wind tunnel can be found in Furieri et al. [12].

The wind tunnel experiments comprised an isolated oblong sand stockpile with the incident wind at  $90^\circ$ . The stockpile was 7.7 cm high, 23.6 cm long and 57.9 cm wide with a  $34.5^\circ$  rest angle. Three ranges of particle size ( $\rho_p = 2630$  kg/m<sup>3</sup>) were used to construct mixtures of erodible and non-erodible particles. It is important to note that one size range, the yellow sand, was erodible or non-erodible depending on the conditions of the experiment (free stream velocity) while two ranges, white (erodible) and black (non-erodible) sands maintains its erodibility under all shear stress conditions. The three size ranges of sand represent three modes of particle size distributions: (1) fine white sand with a diameter varying from 56 to 194  $\mu\text{m}$ , (2) medium yellow sand with a diameter ranging from 300 to 600  $\mu\text{m}$  and (3) black sand with a diameter varying from 700 to 1300  $\mu\text{m}$ . The sand

**Fig. 2** Wind tunnel set-up showing dimensions, camera location and test section. (Adapted from Caliman [3])



color was chosen in order to allow their visual differentiation essential for the use of photographs in the qualitative analysis proposed as a specific objective.

The different sand proportions of the tested stockpiles are presented in Table 1. After weighing the initial mass of the pile, a second weighing was performed at the end of the tests. The subtraction of the initial weight from the final weight gave the amount of emitted mass of sand. A wind tunnel test duration was 15 min, in which pavement develops (pavement effect represents the influence of non-erodible particles on the taking-off of erodible particles). The “pavement effect” is the erodible surface covered by the non-erodible particles, i.e., erodible particles are impeded to take-off) was observed for all cases. Photographs were taken at the beginning of the experiment and every 30 s up to 5 min. Cases D1, E1 and F1 present yellow particles that are non-erodible according to the threshold friction velocity criterion of Shao and Lu [34] for  $7 \text{ m s}^{-1}$ . Cases D2, E2, F2, D3, E3 and F3 have a higher percentage of potentially erodible particles in the size range of the yellow sand particles than previous cited cases.

## 4 Results and discussions

The Results and Discussions section present the following subsections: (1) evaluation of the relationship between the cover rate and the final eroded height (proposed by Caliman [3]) for a multimodal particles size distribution, (2) a comparison between emission estimation and experimental measurements in wind tunnel, (3) an assessment of the protection effect caused by size ranges of potentially (300–600  $\mu\text{m}$ ) erodible and always non-erodible (700–1300  $\mu\text{m}$ ) particles and, (4) a qualitative analysis of particles distribution over the stockpile surface through wind tunnel experiments.

### 4.1 Evaluation of the relationship between the cover rate and the final eroded height

In order to evaluate the validity of the linear relationship between the cover rate and the eroded height for the particle size distribution characteristics, a hypothetical isosurface was assumed for a bed with an area of  $0.1 \text{ m}^2$  and a height of  $0.0025 \text{ m}$ . A scanning of the diameters in each of mode of the particles size distribution for each case

**Table 1** Proportions of sand used in the experiments and initial mass of the piles

Case	Velocity ( $\text{m s}^{-1}$ )	White (%)	Yellow (%)	Black (%)	Initial mass (g)
D1	7	80	12	8	6190.6
D2	8	80	12	8	6190.6
D3	9	80	12	8	6190.6
E1	7	65	21	14	6700.0
E2	8	65	21	14	6700.0
E3	9	65	21	14	6700.0
F1	7	50	30	20	7100.0
F2	8	50	30	20	7100.0
F3	9	50	30	20	7100.0

**Fig. 3** Relationship between the proportion of non-erodible particles covering the surface ( $CR$ ) and the eroded height ( $H$ ) of the hypothetical bed for cases D1, D2 and D3

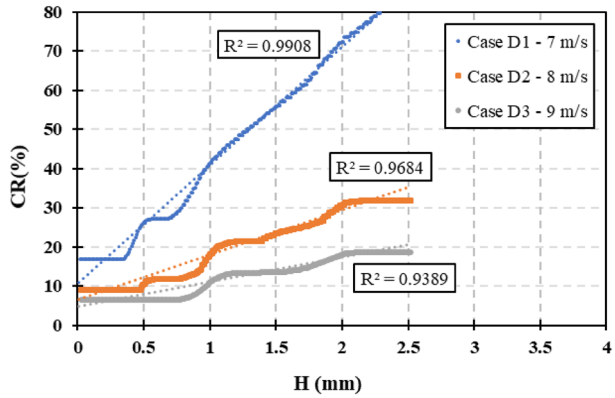
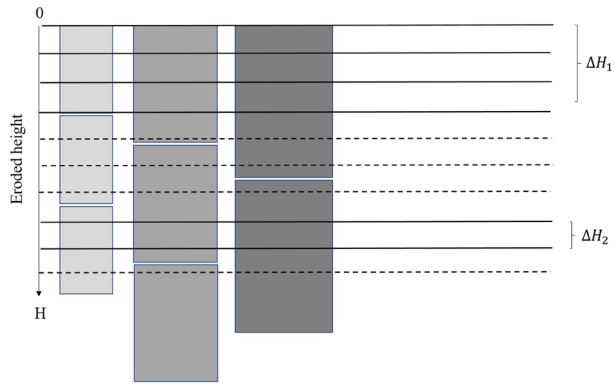


**Fig. 4** Schema of the behavior of the proportion of non-erodible particles covering the surface ( $CR$ ) as a function of the eroded height ( $H$ ). The cover rate remains constant along two eroded heights ( $\Delta H_1$  and  $\Delta H_2$ )



was performed. The cover rate of each non-erodible diameter was added successively to account for the final cover rate and the sum of their diameters counted as the eroded height. The threshold friction velocity ( $u_{*t}$ ) for each diameter was calculated based on Shao and Lu [34] and the surface friction velocity ( $u_*$ ) by Kurose and Komori [23] and Mollinger and Nieuwstadt [29]. The friction velocities calculated for the freestream velocities of 7, 8 and 9 m s<sup>-1</sup> were, 0.30, 0.35 and 0.40 m s<sup>-1</sup>, respectively. Particles of each diameter were considered non-erodible if  $u_* < u_{*t}$ .

Figure 3 shows the results of the procedure described above for cases D1, D2 and D3 (cf. Table 1). Figure 3 also shows the linear fit of the data for each case. Observing the results for the case D1 it is noted that the curve has a horizontal straight line at the beginning, a small positive slope, a second and smaller horizontal straight line and then a long range of data forming an upward line.

To explain this behavior, it is necessary to understand the principles governing the relationship modelled through the approach of the present work. Figure 4 shows the behavior of the cover rate as a function of eroded height for Case D1. The eroded height increases from top to bottom on the vertical axis. The cover rate is accounted for by the area viewed from the top of the particles for a given eroded height. The solid lines show the eroded height at which the cover rate remains constant.



If the eroded height  $H$  is zero, the cover rate  $CR$  is the initial cover rate  $CR_i$ . As  $H$  increases, it is noted that the  $CR$  remains constant until it reaches a height equivalent to the height of the smallest non-erodible diameter. The cover rate remains constant along height  $\Delta H_1$  which corresponds to the first horizontal line seen in Fig. 3. The continuity of erosion leads to the increase of  $H$ . The cover rate increases over the bed surface, resulting in the first positive slope in Fig. 3. With a further increase of  $H$ , a range of heights is again observed where the cover rate is constant ( $\Delta H_2$ ). This second range of  $H$  where  $CR$  is constant gives rise to the second horizontal line of Fig. 3. As the particle size increases within the particle size distribution, the diameters larger than the smaller non-erodible diameter appears more frequently, so this constant  $CR$  region grows to such a point that no other region of constant  $CR$  can be observed, resulting in the long data range forming the second rising line in Fig. 3.

Comparing cases D1, D2 and D3 in Fig. 3, one of the differences is that the initial horizontal lines presented in the curves become larger with a velocity increase. As velocity increases, more yellow particles of smaller diameter become erodible, shifting the first non-erodible diameter to higher values, resulting in higher  $\Delta H$  where  $CR$  is constant.

Figure 5 shows the results for the cases D1, E1 and F1 ( $7 \text{ m s}^{-1}$ ), for the different proportions of sand used. At  $7 \text{ m s}^{-1}$  only a very small portion of the yellow sand is erodible, so the initial cover rate is slightly less than the sum of the proportions of the yellow and black sands: 20%, 35% and 50% for cases D1, E1 and F1, respectively. D1 has the lowest amount of non-erodible particles in the mixture, so it has the lowest cover rate. For this reason, the final eroded height is almost the same as the total height of the bed. Since there is a small amount of non-erodible particles in each layer, it is necessary to armor most of the bed. The F1 case is the one with the most non-erodible particles, resulting in the highest cover rate (Fig. 5). As opposed to case D1, the final eroded height is much smaller than the total height of the bed, because there are many non-erodible particles in each layer, it is not necessary to uncover many layers until the bed is mostly covered by non-erodible particles. Figure 5 also shows that larger proportions of yellow and black (non-erodible) particles lead to steeper slopes, because in this situation the initial cover rate is higher. This is an expected result according to Eq. (4). Similar analysis to those described above can be performed for the other cases presented in Fig. 6.

For the curves, in all cases it is mathematically permissible to make a linear adjustment of the data given the high value for  $R^2$  found (similar results were experimentally obtained by Caliman [3]). Table 2 presents the slope and the initial cover rate obtained by Eqs. (4)

**Fig. 5** Relationship between the proportion of non-erodible particles covering the surface ( $CR$ ) and the eroded height ( $H$ ) of a hypothetical bed for cases D1, E1 and F1 ( $7 \text{ m s}^{-1}$ )

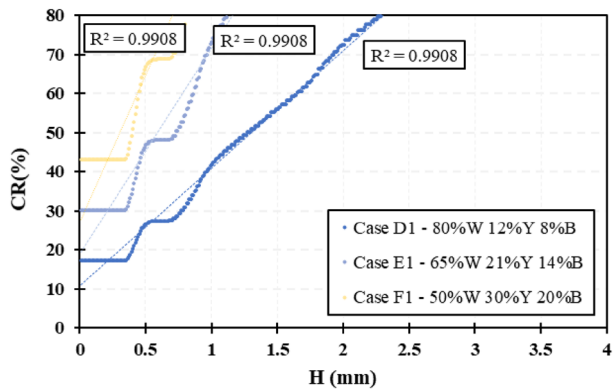


**Fig. 6** Relationship between the proportion of non-erodible particles covering the surface ( $CR$ ) and the eroded height ( $H$ ) of a hypothetical bed for **a** cases E and **b** cases F

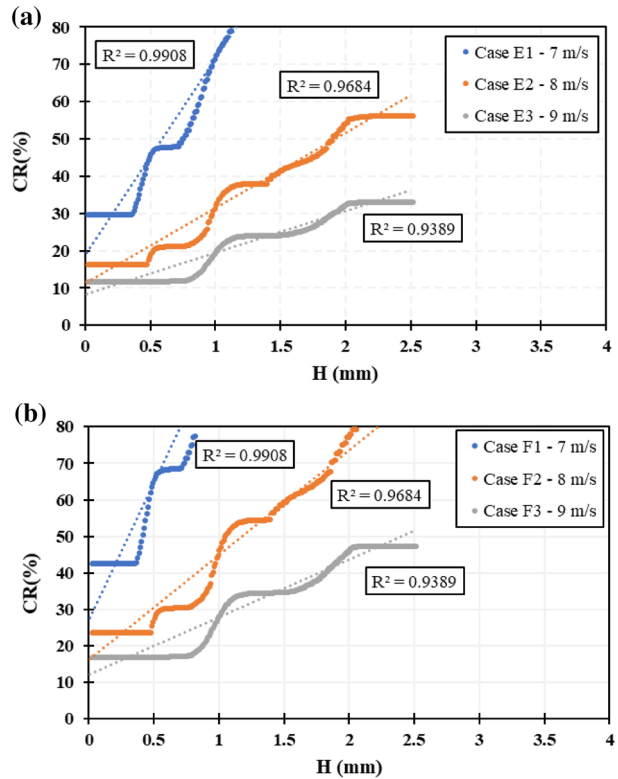


**Table 2** Slope ( $\alpha$ ) and initial cover rate ( $CR_i$ ) calculated and obtained by adjustment

	$D_{NE}$ (mm)	$\varphi$	$\alpha_{NE}$	$CR_i$			$\alpha$		
				Calculated	Adjusted	Error (%)	Calculated	Adjusted	Error (%)
D1	0.7	0.5156	0.1979	10.20	10.77	5.5	14.58	30.11	107
E1	0.8	0.5580	0.3463	19.32	18.84	2.5	24.15	52.70	118
F1	0.9	0.5913	0.4948	29.26	26.91	8.0	32.51	75.28	132
D2	0.7	0.5156	0.1515	7.81	6.46	17.3	11.16	11.51	3
E2	0.8	0.5580	0.2651	14.79	11.3	23.6	18.49	20.14	9
F2	0.9	0.5913	0.3789	22.40	16.14	28.0	24.89	28.78	16
D3	0.7	0.5156	0.0837	4.32	4.78	10.8	6.17	6.35	3
E3	0.8	0.5580	0.1465	8.17	8.36	2.3	10.22	11.12	9
F3	0.9	0.5913	0.2093	12.38	11.94	3.5	13.75	15.89	16

and (5), respectively, and those obtained by linear adjustment of the curves of the relationship between the cover rate and the eroded height for each case. As the hypothetical isosurface considered is from the stockpile and given the volume ( $V_{pile} = 0.0045 \text{ m}^3$ ), the specific mass of the particles ( $\rho_p = 2630 \text{ kg/m}^3$ ) and the initial mass  $m_p$  used in each case (Table 1),  $\varphi$  assumed equal to 1 in Eq. (5), can now be calculated as:  $\varphi = (\rho_p/m_p)/V_{pile}$ .

The results presented in Table 2 show that the relative error between  $CR_i$  calculated by Eq. (5) and  $CR_i$  from a linear fitting varies greatly in each case. The cases at 8 m/s (cases 2) presented the highest values reaching 28%. The angular coefficient  $a$ , calculated by Eq. (4), presents errors larger than 100% at 7 m/s and a maximum value of 16% in the other cases. The high levels of relative error found at 7 m/s for  $a$  can be attributed to the difference between the initial cover rate of the curve and initial cover rate of the adjustment.

Thus we can conjecture that these results are in good agreement with what was proposed by Caliman [3] for the cases considered in the present study, revealing that the linear relationship between the cover rate and the final eroded height can still be considered valid even with the inclusion of another range of non-erodible sizes with variable erodibility (i.e., a multimodal particle size distribution). Consideration of a further range of variable erodibility sizes, in general, changes the cover rate and displaces the non-erodible mean diameter value.

#### 4.2 Comparison between emission estimation and experimental data

The emission model for stockpiles was applied using the constants  $A$ ,  $M$  and  $N$  calculated by Caliman [3]. The results are shown in Table 3. It is possible to observe error levels ranging from 56 to 76%. Despite this, the results of the model followed the same physical pattern of the experimental results. With the increase of the initial proportion of non-erodible particles, at the same rate (cases 1, for example), the amount of removed mass decreases, evidencing that the increase in the presence of larger particles creates a protection effect in which less erodible particles are lost.

Also, increasing the velocity, with the same initial proportion of non-erodible particles (cases D1, D2 and D3, for example), the amount of mass removed increased, indicating that at higher velocities more particles become erodible.

These observed patterns suggest that the physical tendency of the erosion phenomenon was well modeled. Considerations made in the conception and application of the model, such as uniform distribution of the particles along the bed height, homogeneous distribution of the particles on the pile surface, and not considering changes in pile form with erosion propagate quantitative errors in the proportions shown in Table 3.

**Table 3** Comparison between experimental and mathematical model results

Case	$U_\infty$ (m/s)	$\varphi$	$\alpha_{NE}$	Emitted mass (g)		
				Exp.	Mod.	Error (%)
D1	7	0.5156	0.1979	175.5	76.6	56
E1	7	0.5580	0.3463	129.3	45.0	65
F1	7	0.5913	0.4948	116.0	28.4	76
D2	8	0.5156	0.1515	278.5	114.4	59
E2	8	0.5580	0.2651	269.5	72.2	73
F2	8	0.5913	0.3789	153.9	50.5	67
D3	9	0.5156	0.0837	434.5	152.1	65
E3	9	0.5580	0.1465	415.7	103.6	75
F3	9	0.5913	0.2093	280.2	78.6	72

### 4.3 Protection effect of non-erodible particles with different particle size distribution

To evaluate the protective effect of a multimodal distribution of non-erodible particles diameters, a comparison was performed between bimodal experimental data (only fine white and thick black sand) and those already discussed previously in the present work (a mixture of white, yellow and black sands). Table 4 shows the emitted mass from the two wind tunnel measurements carried out at the same conditions of incident fluid flow.

The comparison is made for the main stream velocity equal to  $7 \text{ m s}^{-1}$ . At  $7 \text{ m s}^{-1}$  the yellow sand is predominantly non-erodible. The cases presenting a bimodal particle size distribution are called here D0, E0 and F0.

At  $7 \text{ m s}^{-1}$ , case D1 shows that about 20% of the sand mixture is non-erodible, but 12% is sand with smaller diameters than case D0. This composition results in mass loss of 175.5 g. Comparing with case D0, the mass loss was about 135.4 g. This suggests that the sand mixture D1 has smaller diameters (i.e., 300–1300  $\mu\text{m}$ ) in the non-erodible fraction creating a less effective protection condition when compared to the same proportion of a mixture composed of only a more limited size range (i.e., 700–1300  $\mu\text{m}$ ) of non-erodible particles.

In addition, higher emission may have occurred due to the observed behavior of the yellow sand particles during the experiment. It was observed that some of the yellow particles rolled from stockpile surfaces during testing and moved out of the weighing region. Therefore, they were not suspended, but were recorded as emitted mass. Thus, not every emitted mass increase can be credited to the lower protective effect created. But in any case, this increase is due to the presence of different non-erodible particles size distribution on the mixture.

The same analysis can be made for the other proportions emphasizing what was discussed above. It is worth noting that for cases E0–E1 and F0–F1 the difference in the emitted mass is more important as the amount of yellow sand becomes higher, which supports the physical behavior explained above.

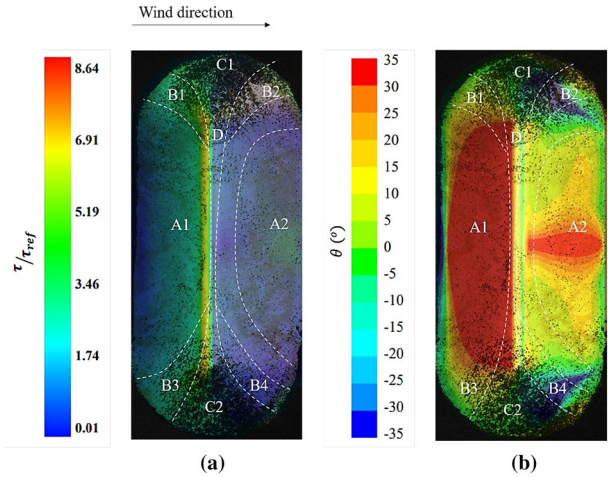
### 4.4 Particle distribution over the stockpile surface

The particle distribution over the stockpile surface is conditioned by the angle of velocity vectors of the wind flow over the surface and the friction velocity. Figure 7a shows the shear stress (normalized by a reference value— $\tau_{ref}$  of undisturbed wind flow over a smooth surface) and Fig. 7b presents the stockpile slope distribution for the case D2 in its final stage of erosion, i.e., after the pavement is completely formed.

**Table 4** Comparison between experimental data at  $7 \text{ m s}^{-1}$

Case	White (%)	Yellow (%)	Black (%)	Emitted mass (g)
D0	80	0	20	135.4
E0	65	0	35	48.7
F0	50	0	50	10.9
D1	80	12	8	175.5
E1	65	21	14	129.3
F1	50	30	20	116.0

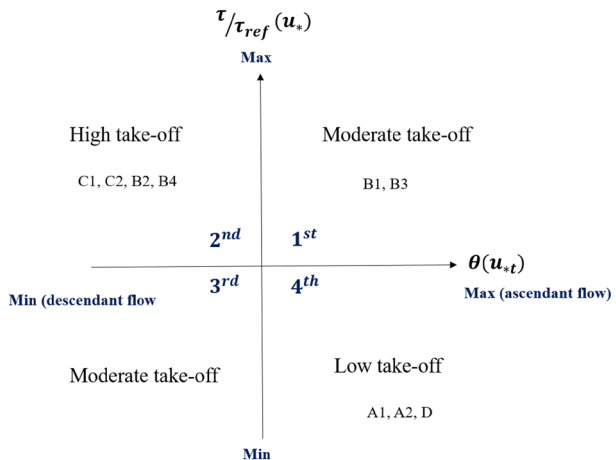
**Fig. 7** **a** Shear stress distribution and **b** angle of velocity vectors of wind flow distribution over the stockpile at the final stage of erosion from Caliman [3] overlapping to the D2 case image of the experiments from the present work



Both distributions of  $\tau/\tau_{ref}$  and  $\theta$  were obtained through numerical simulations of the turbulent wind flow representing the same characteristics of fluid flow found in the wind tunnel used for the present work. The three-dimensional equations of mass and momentum conservation are solved using the commercial software Fluent 15.0. The  $k-\omega$  Shear Stress Transport (SST) model is used to incorporate turbulence effects. The inlet boundary conditions take into account velocity, turbulent kinetic energy and specific dissipation rate. Fully developed flow is assumed for the outflow conditions. Symmetry conditions are applied to the upper boundary of the domain and finally, for lateral boundaries, ground and pile surface, no-slip conditions are imposed. Further details of the numerical simulations conditions are presented in Caliman [3].

To better understand what Fig. 7 shows, a quadrants analysis (Fig. 8) was made based on the variables  $\tau/\tau_{ref}$  and  $\theta$  that are dependent on  $u_{*}$  and  $u_{*t}$ , respectively, to assess the particles take-off. The larger the values of slope  $\theta(u_{*t})$ , the greater the emission criterion (i.e., increased value of threshold friction velocity). This occurs because the flow in these regions (red scale of  $\theta$  shown in Fig. 7) is ascending on the windward face of the stockpile,

**Fig. 8** Quadrants analysis for the variables  $\tau/\tau_{ref}$  and  $\theta$  to assess the particles take-off



which is contrary to the gravity force acting on the particles over the inclined surface. So,  $u_{*c}$  is smaller than  $u_{*t}$  and the particles do not take off. The larger the values of shear stress  $\tau/\tau_{ref}(u_*)$ , the greater the friction velocity (red scale of  $\tau/\tau_{ref}$  shown in Fig. 7). So,  $u_{*c}$  exceeds the value of  $u_{*t}$  causing the particles take-off.

The effects of  $\theta(u_{*t})$  and  $\tau/\tau_{ref}(u_*)$  on particle take-off phenomena are compared simultaneously in Fig. 8. It is noticed that when the two variables tends towards to its maximum or minimum values, the effects are counterbalanced and there is moderate particle take-off (first and third quadrant Fig. 8). Regions B1 and B3 presents this behavior meaning that some part of the particle size distribution can be emitted.

When  $\theta(u_{*t})$  tends towards its maximum and  $\tau/\tau_{ref}(u_*)$  tend towards its minimum, more shear stress is required than actually exists on the surface of the stockpile to initiate particle entrainment. So, there is low particle loss (fourth quadrant of Fig. 8). Regions A1 and D for the D2 case in Fig. 9 do not show significant changes on the surface particle distribution when initial and final states are compared. On the other hand, when  $\tau/\tau_{ref}(u_*)$  tends towards to its maximum and  $\theta(u_{*t})$  tend towards to its minimum, there is sufficient shear stress on the surface of the stockpile (high values of  $\tau/\tau_{ref}(u_*)$ ) where the flow is descending (negative values of  $\theta(u_{*t})$ ). So, there is high particle take-off (second quadrant of Fig. 8). Regions C1, C2, B2 and B4 present greater numbers of non-erodible black particles because they were strongly eroded.

The A2 region is a recirculation zone. The flow ascends in the central region (high values of  $\theta(u_{*t})$ ) subjected to a moderated shear stress and descends on the sides (moderated values of  $\theta(u_{*t})$ ) subjected to a low shear stress forming a vortex. So, in this zone there is a low take-off.

**Fig. 9** Initial and final stages of erosion for all tested cases

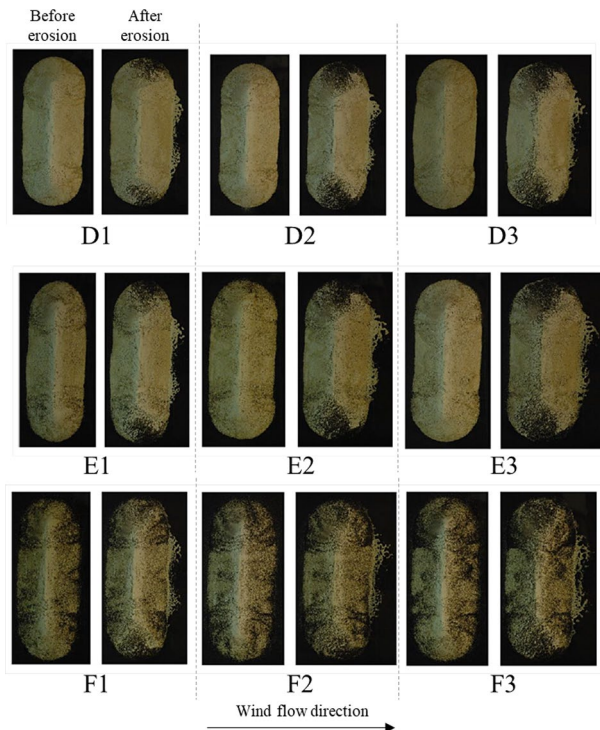


Figure 9 shows the initial and final erosion stages for all cases. The same analysis described above can be performed for the other cases. The difference here is that with the increase in velocity and the initial proportion of yellow and black particles the observed effects occurred with greater intensity in larger regions of non-erodible particles accumulation.

The cases F shown in Fig. 9 present a different behavior from the others. The proportion of yellow and black particles was such that there was little difference between the initial and final stages, although the freestream velocity was higher. This shows that the higher the proportion of non-erodible particles, the greater the protection effect observed, the smaller the amount of particles emitted and the smaller the observed changes in the surface of the pile.

## 5 Conclusions

The present work attempted to: (1) evaluate the linearity of the relation between the cover rate and the eroded height also considering the role of particle size distribution to influence erodibility, (2) validate the results of the model for the presence of a third size range of non-erodible particle sizes with variable erodibility, (3) evaluate the protective effect of multimodal distribution of particles diameters and (4) qualitatively evaluate the final surface particle size distribution of an experimental oblong stockpile composed of granular materials.

The relationship between the cover rate and the eroded final height can be considered linear for particle size distribution ranges and velocities tested. The Caliman [3] model emission results match experimental results with, however, significant errors. The uniform distribution of the particles along the bed height, the homogeneous distribution of the particles on the surface of the pile and no consideration of the changes of the pile shape with erosion, may have influenced the results of the model. However, modeled emission presented the same physical trend of emissions experimentally measured.

The algebraic emission model evaluated through the present work may be, even at the current stage of development, a very useful tool for quantifying the wind erosion of open yards of storage piles on industrial sites. The mathematical model works well in comparative analysis between scenarios, but not in absolute values. As the velocity increases, using the same proportion of non-erodible particles, emissions increase, because more particles are entrained. When evaluating the increase in the proportion of non-erodible particles at the same freestream velocity, it was observed that less particles were emitted as the surface becomes progressively armoured with larger non-erodible particles. Therefore, the model has physical basis for real case applications. It requires further investigation into why the emitted mass was under-estimated.

The protective effect is altered if a third mode of non-erodible particle diameters is present (300–1300  $\mu\text{m}$ ). This third mode is non-erodible for wind  $< 7 \text{ m s}^{-1}$  becoming erodible as wind speed exceeds this value. It created less effective protection for the pile. When the results were compared to the same proportion of a mixture composed of only one mode of non-erodible particle size distribution with larger diameter (700–1300  $\mu\text{m}$ ) the emitted mass was larger.

The qualitative analysis of the images of the experiments showed that the distribution of particles under the surface of the pile can be explained qualitatively by the implicit



evaluation of the threshold condition that considers both the bed angle and the friction velocity over the stockpile surface.

**Acknowledgements** This work was carried out with the financial support of CAPES and CNPq.

## References

1. Badr T, Harion J-L (2005) Numerical modelling of flow over stockpiles: implications on dust emissions. *Atmos Environ* 39(30):5576–5584. <https://doi.org/10.1016/j.atmosenv.2005.05.053>
2. Badr T, Harion J-L (2007) Effect of aggregate storage piles configuration on dust emissions. *Atmos Environ* 41(2):360–368. <https://doi.org/10.1016/j.atmosenv.2006.07.038>
3. Caliman MFSC (2017) Influence of non-erodible particles on wind erosion. Doctoral thesis. Universidade Federal do Espírito Santo, Vitória, ES
4. Cong X, Yang S, Cao S, Chen Z, Dai M, Peng S (2012) Effect of aggregate stockpile configuration and layout on dust emissions in an open yard. *Appl Math Model* 36(11):5482–5491. <https://doi.org/10.1016/j.apm.2012.01.014>
5. Crawley D, Nickling W (2003) Drag partition for regularly-arrayed rough surfaces. *Bound-Layer Meteorol* 107(2):445–468. <https://doi.org/10.1023/a:1022119909546>
6. Derakhshani SM, Schott DL, Lodewijks G (2013) Dust emission modelling around a stockpile by using computational fluid dynamics and discrete element method. *AIP Conf Proc* 1542(2013):1055–1058. <https://doi.org/10.1063/1.4812116>
7. Descamps I, Harion J-L, Baudoin B (2005) Taking-off model of particles with a wide size distribution. *Chem Eng Process* 44(2):159–166. <https://doi.org/10.1016/j.cep.2004.04.007>
8. Diego I, Pelegrý A, Torno S, Toraño J, Menendez M (2009) Simultaneous CFD evaluation of wind flow and dust emission in open storage piles. *Appl Math Model* 33(7):3197–3207. <https://doi.org/10.1016/j.apm.2008.10.037>
9. Dong Z, Wang H, Liu X, Wang X (2004) A wind tunnel investigation of the influences of fetch length on the flux profile of a sand cloud blowing over a gravel surface. *Earth Surf Process Landf* 29(13):1613–1626. <https://doi.org/10.1002/esp.1116>
10. Faria R, Ferreira AD, Sismeiro JL, Mendes JCF, Sousa ACM (2011) Wind tunnel and computational study of the stoss slope effect on the aeolian erosion of transverse sand dunes. *Aeol Res* 3:303–314. <https://doi.org/10.1016/j.aeolia.2011.07.004>
11. Ferreira AD, Pinheiro SR, Francisco SC (2013) Experimental and numerical study on the shear velocity distribution along one or two dunes in tandem. *Environ Fluid Mech* 13:557–570. <https://doi.org/10.1007/s10652-013-9282-7>
12. Furiere B, Russeil S, Santos JM, Harion J-L (2013) Effects of non-erodible particles on aeolian erosion: wind-tunnel simulations of a sand oblong storage pile. *Atmos Environ* 79:672–680. <https://doi.org/10.1016/j.atmosenv.2013.07.026>
13. Furiere B, Harion JL, Milliez M, Russeil S, Santos JM (2013) Numerical modelling of aeolian erosion over a surface with non-uniformly distributed roughness elements. *Earth Surf Proc Land* 39(2):156–166. <https://doi.org/10.1002/esp.3435>
14. Furiere B, Santos JM, Russeil S (2014) Aeolian erosion of storage piles yard: contribution of the surrounding areas. *Environ Fluid Mech* 14:51–67. <https://doi.org/10.1007/s10652-013-9293-4>
15. Gillette D, Stockton P (1989) The effect of nonerodible particles on wind erosion of erodible surfaces. *J Geophys Res Atmos* 94(D10):12885–12893. <https://doi.org/10.1029/JD094iD10p12885>
16. Gillies J, Nickling W, King J (2007) Shear stress partitioning in large patches of roughness in the atmospheric inertial sublayer. *Bound-Layer Meteorol* 122(2):367–396. <https://doi.org/10.1007/s10546-006-9101-5>
17. Gillies JA, Green H, McCarley-Holder G, Grimm S, Howard C, Barbieri N, Ono D, Schade T (2015) Using solid element roughness to control sand movement: Keeler Dunes, Keeler, California. *Aeolian Res* 18:35–46. <https://doi.org/10.1016/j.aeolia.2015.05.004>
18. Hoonhout BM, De Vries S (2016) A process-based model for aeolian sediment transport and spatiotemporal varying sediment availability. *J Geophys Res Earth Surf* 121:1555–1575. <https://doi.org/10.1002/2015JF003692>
19. Iversen J, Wang W, Rasmussen K, Mikkelsen H, Leach R (1991) Roughness element effect on local and universal saltation transport. In: Barndorff-Nielsen O, Willetts B (eds) *Aeolian grain transport: acta mechanica supplementum*, vol 2. Springer, Vienna, pp 65–75



20. Iversen J, Rasmussen K (1994) The effect of surface slope on saltation threshold. *Sedimentology* 41(4):721–728. <https://doi.org/10.1111/j.1365-3091.1994.tb01419.x>
21. Klose M, Shao Y, Li X, Zhang H, Ishizuka M, Mikami M, Leys JF (2014) Further development of a parametrization for convective turbulent dust emission and evaluation based on field observations. *J Geophys Res Atmos* 119(17):10441–10457. <https://doi.org/10.1002/2014JD021688>
22. Kok J, Mahowald N, Fratini G, Gillies J, Ishizuka M, Leys J, Mikami M, Park M-S, Park S-U, Van Pelt R, Zobeck T (2014) An improved dust emission model—Part 1: model description and comparison against measurements. *Atmos Chem Phys* 14(23):13023–13041. <https://doi.org/10.5194/acp-14-13023-2014>
23. Kurose R, Komori S (2001) Turbulence structure over a particle roughness. *Int J Multiph Flow* 27(4):673–683. [https://doi.org/10.1016/S0301-9322\(00\)00044-6](https://doi.org/10.1016/S0301-9322(00)00044-6)
24. Lyles L, Allison B (1975) Wind erosion: the protective role of simulated standing stubble. *Am Soc Agric Eng* 19(1):61–64
25. Marshall J (1971) Drag measurements in roughness arrays of varying density and distribution. *Agric Meteorol* 8:269–292. [https://doi.org/10.1016/0002-1571\(71\)90116-6](https://doi.org/10.1016/0002-1571(71)90116-6)
26. Marticorena B, Bergametti G (1995) Modeling the atmospheric dust cycle: 1. Design of a soil-derived dust emission scheme. *J Geophys Res Atmos* 100(D8):16415–16430. <https://doi.org/10.1029/95JD00690>
27. McKenna Neuman C, Nickling W (1995) Aeolian sediment flux decay: nonlinear behaviour on developing deflation lag surfaces. *Earth Surf Proc Land* 20(5):423–435. <https://doi.org/10.1002/esp.3290200504>
28. Miri A, Dragovich D, Dong Z (2017) Vegetation morphologic and aerodynamic characteristics reduce aeolian erosion. *Nat Sci Rep* 7:12831. <https://doi.org/10.1038/s41598-017-13084-x>
29. Mollinger A, Nieuwstadt F (1996) Measurement of the lift force on a particle fixed to the wall in the sublayer of a fully developed turbulent boundary layer. *J Fluid Mech* 316:285–306. <https://doi.org/10.1017/S0022112096000547>
30. Musick HB, Gillette DA (1990) Field evaluation of relationships between a vegetation structural parameter and sheltering against wind erosion. *Land Degrad Dev* 2(2):87–94. <https://doi.org/10.1002/ldr.3400020203>
31. Nickling W, McKenna Neuman C (1995) Development of deflation lag surfaces. *Sedimentology* 42(3):403–414
32. Novak L, Bizjan B, Pražnikar J, Horvat B, Orbanić A, Širok B (2015) Numerical modeling of dust lifting from a complex-geometry industrial stockpile. *J Mech Eng* 61(11):621–631. <https://doi.org/10.5545/sv-jme.2015.2824>
33. Raupach M, Gillette D, Leys J (1993) The effect of roughness elements on wind erosion threshold. *J Geophys Res Atmos* 98(D2):3023–3029. <https://doi.org/10.1029/92JD01922>
34. Shao Y, Lu H (2000) A simple expression for wind erosion threshold friction velocity. *J Geophys Res Atmos* 105(D17):22437–22443. <https://doi.org/10.1029/2000JD900304>
35. Tan L, Zhang W, Qu J, Zhang K, An Z, Wang X (2013) Aeolian sand transport over gobi with different gravel coverages under limited sand supply: a mobile wind tunnel investigation. *Aeol Res* 11:67–74. <https://doi.org/10.1016/j.aeolia.2013.10.003>
36. Turpin C, Badr T, Harion J-L (2010) Numerical modelling of aeolian erosion over rough surfaces. *Earth Surf Proc Land* 35(12):1418–1429. <https://doi.org/10.1002/esp.1980>
37. US Environmental Protection Agency (2006) Miscellaneous Sources. *Industrial Wind Erosion*. AP-42
38. Zou X, Zhang C, Cheng H, Kang L, Wu Y (2015) Cogitation on developing a dynamic model of soil wind erosion. *Earth Sci* 58(3):462–473. <https://doi.org/10.1007/s11430-014-5002-5>